Analysis and design optimisation of innovative waste-heat recovery units in a steel production plant

Francesco Tosto[a], Sanjay Vermani[a], Joke Bauwens[b], Bart Vervaet[c], Carlo De Servi[a,d] and Nitish Anand[a]

[a] *Flemish Institute for Technological Research, Boeretang, Belgium, e-mail: francesco.tosto@vito.be,*
[b] *ArcelorMittal Belgium, Gent, Belgium*
[c] *CRM Group, Zwijnaarde, Belgium*
[d] *Delft University of Technology, Delft, Netherlands*

Abstract:

Steel production is a highly energy-intensive process that generates a substantial amount of waste heat. Recovering this thermal energy enables a reduction of carbon dioxide emissions and supports the realization of circular energy systems, in which, for instance, surplus thermal energy from industry is supplied for heating purposes to surrounding buildings and communities using district heating networks. This study evaluates two complementary technologies to efficiently recover waste energy from the hot strip mill of a steel production plant. More specifically, a removable conductive heat block that can be placed on top of the coils and a water-cooled panel to absorb the radiative heat emitted by the coil during transfer are investigated. To assess the effectiveness of these two solutions, the heat recovery systems were simulated using first-principles component models, in order to estimate both their energy recovery potential and to obtain a preliminary design of the heat transfer devices. The simulations show that a minimum of 19 GWh of thermal energy can be harvested annually if both solutions are deployed. The design of both the radiative panels and the removable heat exchanger is further improved using topology optimization, with the goal of reducing pressure drop on the cooling water side. The results show that topology-optimized channels enable a reduction in pumping power in both devices by over 26% with respect to the baseline design, thus improving overall system efficiency.

Keywords:
Topology optimisation, waste heat recovery, heat exchanger, system modelling, steel manufacturing.

1. Introduction

Steel production is an energy-intensive industrial activity responsible for about 7% of global anthropogenic emissions [1]. At the same time, a substantial share of thermal energy is still discharged as waste heat. Recovering even a fraction of this energy would improve plant efficiency, reduce related CO_2 emissions, and support more circular heat use, e.g., through integration with district-heating systems [2].

Waste-heat recovery in the steel production processes has traditionally focused on more conventional and stationary sources, such as process off-gases, furnaces and cooling circuits, while hot intermediate and final products remain more difficult to exploit because of their intermittent availability, complex logistics and severe thermal conditions. Recent industrial developments have therefore increased interest in heat-recovery concepts specifically tailored to unconventional steel manufacturing processes, as highlighted for the manufacturing of extruded steel wires [2].

In the case of hot-rolled steel coil production, each coil leaves the hot-strip mill at high temperature ($\sim 600\,^{\circ}\mathrm{C}$) and releases a significant amount of sensible heat during transport and storage, thus offering a promising, previously untapped source for heat recovery. Two approaches can be identified

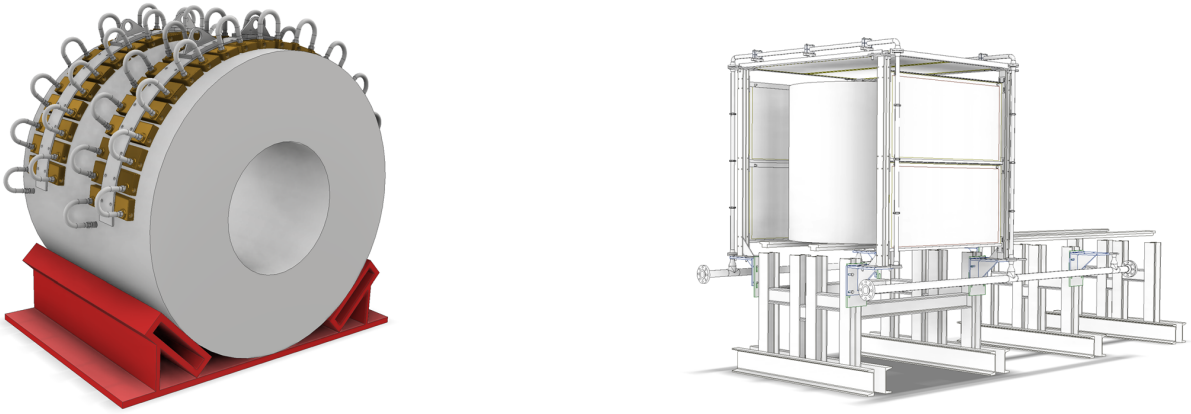

(a) (b)

Figure 1: Qualitative mock-up of the conductive heat-recuperation unit for coil cooling (a) and the radiative heat-recuperation unit installed in the transport tunnel (b). Courtesy of CRM Group.

for waste heat recovery. The first option is to recover the radiative heat emitted by the hot steel coils, for example, by means of radiative panels installed along the transport tunnel. The second option is to recover heat directly from the steel coil itself via thermal contact with a water jacket. Although the two approaches seem promising, a quantitative assessment of the total amount of heat that can be recovered and its impact on the steel production plant is unknown. Furthermore, the design and performance of such devices depend not only on the heat transfer but also on hydraulic losses, operational constraints and manufacturability.

This work proposes a modelling and design framework for two heat-recovery concepts, namely a conductive recuperation unit and a radiative recuperation unit. To this end, a two-step approach is proposed, combining system-level design and CFD-based optimisation. First, system-level modelling is used to estimate the heat recovery potential, size the main components, and assess their performance. For this purpose, both concepts are modelled using an in-house Modelica library developed for the sizing and simulation of heat transfer systems. Once a feasible baseline design is established, further performance improvements are pursued through computational fluid dynamics (CFD) density-based topology optimisation of the heat-recovery units. This method has emerged as a powerful approach for fluid and thermal systems, enabling the systematic design of channels, manifolds and heat-transfer surfaces [3–5] with improved flow distribution and reduced pressure losses.

The paper is organised as follows. Section 2. presents the reduced-order system models developed for both heat-recuperation units investigated in this study and the key results. Section 3. describes the methodology used to optimise the design of their key components and discusses the corresponding results. Finally, Section 4. summarises the main conclusions of the study.

2. System modelling

2.1. Conductive heat-recuperation unit

Figure 1 shows the conductive heat-recuperation unit developed for deployment in the coil yard at ArcelorMittal Belgium (AMB). The unit is designed to recover heat from high-temperature steel coils while simultaneously accelerating coil cooling. Each conductive branch consists of a series of brass blocks connected by a metallic elastic strip, as shown in Figure 1a. The number of branches that can be installed on a coil depends on the coil geometry; for a regular-sized coil at AMB, up to four conductive strips can be placed on the upper surface, see Figure 1a. A supply manifold (not shown in the figure) distributes cold water from the return line of the district-heating network to the individual branches. Within each branch, the water flows through the serpentine passage that maximises thermal contact and residence time. The heated water is then collected in an outlet manifold and discharged

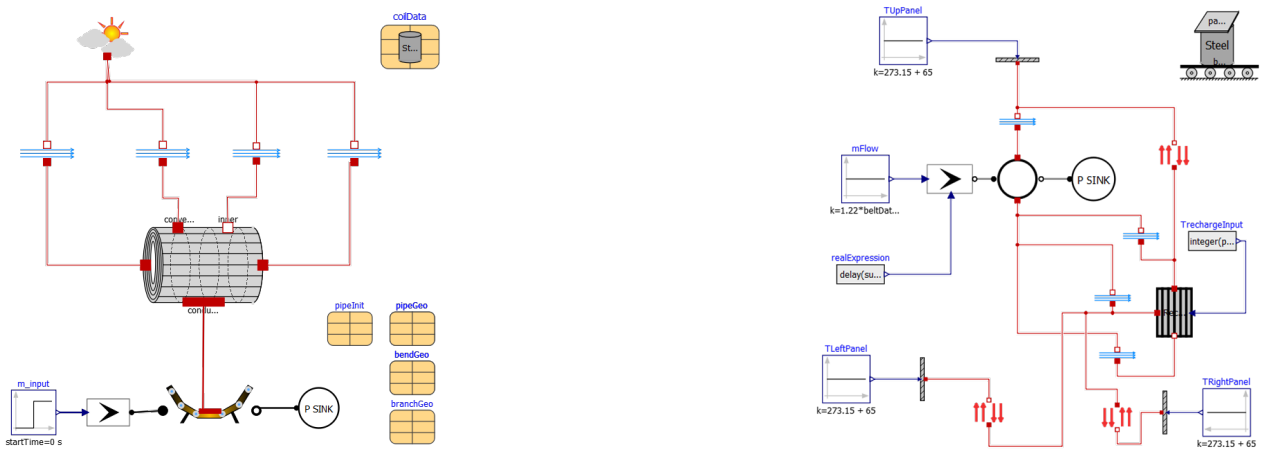

(a) (b)

Figure 2: System models of the conductive (a) and radiative (b) heat-recuperation units.

to the district-heating circuit.

The system has been sized subject to both manufacturing and operational constraints. To limit production costs, all conductive blocks within a branch share the same geometry and dimensions. Each block is made of brass and measures $350 \times 100 \times 34$ mm. A hollow channel of 22 mm diameter is machined inside each block to allow water circulation and heat extraction.

To assess the performance of the unit, a system-level analysis was carried out. Figure 2a shows the model developed for the conductive concept. The model was implemented in Modelica, which enables acausal modelling of the coupled thermal and hydraulic phenomena. The model consists of a three-dimensional heat-transfer representation of the coil, coupled to a detailed model of the conductive support structure that resolves convective heat transfer in the embedded piping. The system is fully modular, allowing different correlations to be used for natural convection from the coil surface to the ambient and for forced convection inside the serpentine channels. Flow sources and a pressure sink define the hydraulic boundary conditions, while heat flow rate and temperature are exchanged between model components through appropriate connectors. The framework can operate in both steady-state and transient modes, enabling evaluation of nominal performance and simulation of the full coil-cooling process. It should be noted that the largest sources of uncertainty are expected to arise from the thermal contact conductance between coil and blocks, the effective radial conductivity of the wound coil, and the natural-convection boundary conditions. The model should therefore be interpreted primarily as a design and performance-assessment tool rather than a fully resolved predictive model.

To capture the non-uniform heat-transfer behaviour within the coil, its volume is discretised into an arbitrary number of control volumes in the radial (N_r), tangential (N_θ), and axial (N_z) directions, where N_z is taken equal to the number of conductive branches. In the radial direction, the effective thermal conductivity is reduced to one-third of the bulk steel value to account for the air gaps between adjacent coil layers. This correction was derived from internal experimental measurements. For each discretised element, the energy balance is solved in the radial, tangential, and axial directions, allowing the model to reproduce the heterogeneous cooling that characterises industrial steel coils.

The coil is modelled using a transient finite-volume formulation in cylindrical coordinates, accounting for heat conduction in the radial, tangential, and axial directions. Thermophysical properties are assumed constant, with thermal conductivity and heat capacity taken from a material database [6]. Heat losses from the upper, lower, and inner lateral surfaces of the coil are modelled by natural convection, while at the outer lateral surface heat is partly extracted by the recuperation unit and partly dissipated to the ambient. Natural-convection heat transfer is evaluated using the correlations of Mills [7] and Churchill and Chu [8]. Within the recuperation unit, heat conduction through the brass blocks is

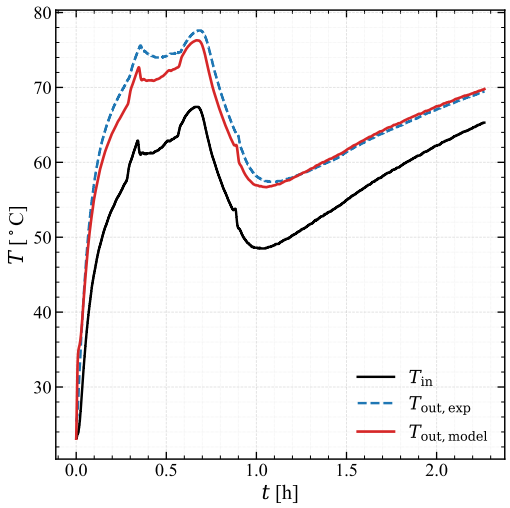

(a)

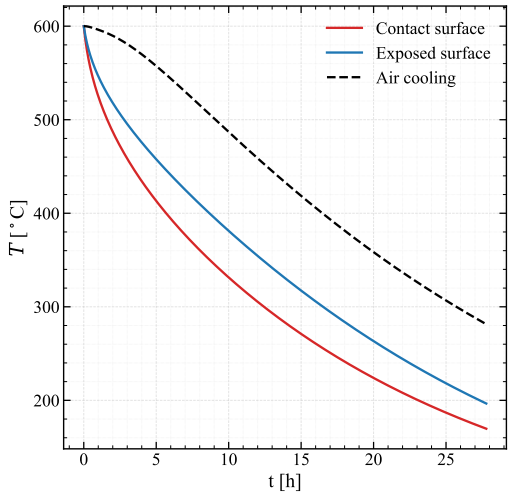

(b)

Figure 3: (a) Experimental validation of the system model: outlet-water temperature vs time. (b) Results of the system-level analysis: coil-surface temperature during cooling. The temperature trend for the air cooling process is also plotted.

described by Fourier's law, and convective heat transfer to the water is modelled using standard correlations for heated internal flows, namely the Gnielinski correlation [9]. Imperfect thermal contact between the coil and the recuperation unit is represented through a thermal contact conductance determined from internal experimental measurements. The pressure drop inside the channel machined within each block is calculated using the Colebrook–White correlation [10], while the additional pressure losses in the bends connecting adjacent blocks are evaluated using an experimental correlation from VDI [9].

The boundary conditions are defined to match the return conditions of the district-heating network. In particular, an inlet water temperature of $54.5\,^{\circ}\mathrm{C}$ is prescribed, while the initial coil temperature is set to $600\,^{\circ}\mathrm{C}$. The mass flow rate is sized according to energy conservation and preliminary estimations of the heat transferred to the fluid. Calculations have been conducted for a representative 1.8m high coil of 1.8m of diameter. The simulations were performed in OMEdit over a time horizon of $t \in [0,\ 100{,}000]\ \mathrm{s}$. The output grid consisted of 500 uniform intervals, corresponding to an effective output step of approximately $200\ \mathrm{s}$. Time integration was carried out using the `dassl` solver, a variable-step, variable-order BDF method, with an absolute tolerance of 10^{-6} [11]. Root finding, event restart, and parameter pre-evaluation were enabled to ensure robust treatment of discontinuities and state events. No explicit limits were imposed on the initial or maximum step size.

Figure 3a compares the outlet-water temperature predicted by the system model with experimental measurements obtained on a pilot-scale test set-up developed within the project. The test was carried out on a single branch cooling a small coil initially at $600\,^{\circ}\mathrm{C}$. The measured inlet-water temperature, mass flow rate, and coil-surface temperature were prescribed as boundary conditions in the model. Good agreement is observed between simulation and experiment. After $t = 2.3\ \mathrm{h}$, the deviation in outlet-water temperature is below 1%, whereas larger discrepancies occur during the initial transient, when the inlet temperature varies non-monotonically. The maximum deviation, about 3%, is recorded at $t \approx 0.5\ \mathrm{h}$. Overall, the results indicate that the calibrated model reproduces the transient thermal behaviour of the conductive heat-recuperation unit with satisfactory accuracy.

Table 1a summarises the performance of the conductive unit. It can be observed that an optimal design found comprises four branches and $\sim$ 20 conductive blocks per branch, corresponding to an overall lateral surface coverage of $\sim 40\%$. This configuration was selected to provide sufficient heat-transfer area, achieve a meaningful temperature rise between inlet and outlet water, and maintain adequate contact between the conductive branches and the coil surface. A larger number of blocks per

Table 1: Key performance indicators of the two heat-recuperation units.

(a) Conductive heat-recuperation unit

Parameter	Value	Unit
Pipe serpentine length (per branch)	12.35	m
Number of blocks per branch	21	–
Number of branches	4	–
Water temperature increase (ΔT)	16.39	°C
Heat recovered (per branch)	13	kW
Pressure drop (per branch)	54.81	kPa
Mean flow velocity	0.51	m/s
Mass flow rate (per branch, design)	0.19	kg/s
Mass flow rate (overall, design)	0.76	kg/s

(b) Radiative unit: upper and side panels

Parameter	Upper	Side	Unit
Available heat at panel surface	4.83	7.26	kW
Water temperature increase	20.00	28.04	°C
Panel-to-fluid heat recovery efficiency	98	93	%
Pressure drop	13.83	13.83	kPa

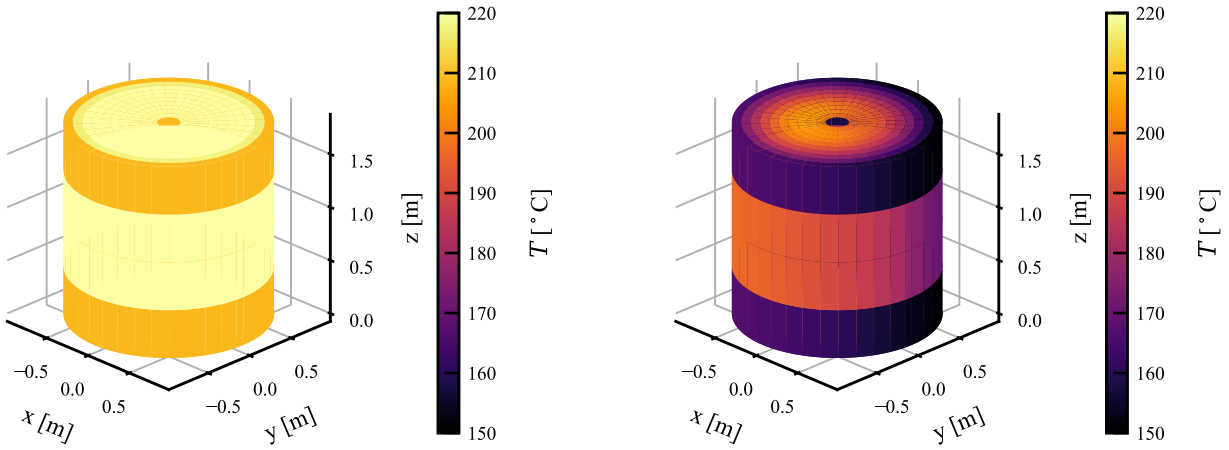

(a) (b)

Figure 4: Coil-surface temperature fields obtained from the system-level analysis after 28 h of cooling: (a) natural cooling in air; (b) cooling assisted by the conductive heat-recuperation unit.

branch would reduce contact quality at the branch extremities, since the branches are simply placed on top of the coil and gravity is the only mechanism ensuring contact. Conversely, fewer blocks would reduce the available heat-transfer area and therefore the overall recovery effectiveness. Under nominal conditions, the system is able to recover 52 kW per coil, corresponding to about 80% of the peak thermal power available at the beginning of the cooling process. As expected, the recovered power decreases over time as the coil surface cools. Assuming 6000 operating hours per year, the annual recoverable energy is 0.312 GWh.

Figure 4 compares the coil-surface temperature fields predicted after 28 h of cooling for two cases: natural cooling in air and cooling assisted by the conductive heat-recuperation unit. The conductive solution produces a markedly non-uniform temperature field because only a fraction of the lateral surface is in direct thermal contact with the recuperation branches. Compared with air cooling alone, the conductive unit accelerates heat removal in the contact regions, resulting in lower local surface temperatures and a stronger circumferential temperature gradient. In particular, a $\Delta T \approx 112\,^{\circ}\mathrm{C}$ at $t = 28$ h is observed between air-cooled and conduction-cooled coils at the surface where the contact occurs, whereas a $\Delta T \approx 85\,^{\circ}\mathrm{C}$ is observed on the exposed surface.

Figure 3b shows the evolution of the coil-surface temperature during the cooling process. The corresponding trend for natural cooling in air is also reported for comparison. Because the conductive unit covers only part of the coil surface, the cooling remains spatially non-uniform throughout the process. After approximately 28 h of operation, the temperature difference between the regions in

contact with the recuperation system and the exposed regions reaches $\sim 27\,^{\circ}\mathrm{C}$. This non-uniformity is further exacerbated by surface oxidation, which reduces the effective thermal conductivity of the coil.

2.2. Radiative heat-recuperation unit

The radiative heat-recuperation unit consists of an array of heat-collecting panels installed inside the transport tunnel between the hot strip mill and the coil yard. These panels are designed to absorb part of the thermal radiation emitted by the hot steel coils and transfer this energy to a working fluid flowing through embedded serpentine piping. The panels are mounted above and alongside the conveyor belt in order to intercept as much radiative heat as possible. To enhance radiative absorption, the exposed surfaces are coated with in-house-manufactured high-emissivity coating materials.

Figure 2 shows a representative tunnel segment comprising six identical radiative panels: four mounted laterally along the sides of the conveyor and two installed above it. Each panel has dimensions of 2×1 m, is made of aluminium, and incorporates a copper serpentine welded to the rear, non-exposed surface. In the proposed concept, these units would be distributed along the full length of the transport tunnel to maximise the overall heat-recovery potential.

As for the conductive concept, a system-level model was developed in Modelica to estimate the heat-recovery potential of the radiative solution. Figure 2b depicts the model for a representative tunnel section. The system consists of a coil module exchanging heat with its surroundings by natural convection to the plenum and by radiation to the upper and lateral panels. Dedicated component models were developed to describe radiative exchange between the coil and the panels, as well as convective heat transfer between the coil and the surrounding air. Although the framework is capable of transient simulations, it was used here only for steady-state analysis.

In contrast to the conductive model presented in Section 2.1., the present model should be regarded primarily as a design and preliminary steady-state performance-assessment tool. The main sources of uncertainty arise from the effective emissivity of the coil surface, the frequency at which coils pass through a given tunnel section, and the thermal contact between the panel surface and the welded serpentine. For this reason, no dedicated validation campaign has yet been carried out for this model.

The coil is modelled as a lumped thermal mass with uniform temperature. Radiative heat transfer between the coil and the panel is described using a radiosity approach, with view factors determined from geometrical correlations available in the literature [7, 12]. Natural convection is modelled using empirical correlations implemented in the component models [7, 8, 13, 14]. The pressure drop in the panel serpentine is evaluated using the same approach adopted for the conductive unit, while the thermal contact between the aluminium panel and the welded serpentine is represented using the correlation proposed by Rane and Tandale [15]. The numerical model and cold-side boundary conditions are the same as those used for the conductive unit.

Table 1b summarises the key performance indicators for the upper and side panels of the radiative heat-recuperation unit. According to the model, each side panel receives up to 7.26 kW from the coil surface, predominantly by radiation, of which approximately 93% is transferred to the water flowing through the serpentine. Each upper panel receives up to 4.83 kW and, in the present configuration, transfers 98% of this heat to the fluid. For the upper panels, about 34% of the heat transferred from the coil is due to natural convection, while the remaining 66% is due to radiation.

Based on these panel-level results, the total heat recovered by the fluid can be estimated by scaling the recovered power of the individual panels to the full tunnel layout. Assuming 60 radiative heat-recuperation units distributed along the tunnel, the overall recoverable thermal power is estimated at 2.19 MW, corresponding to 13.1 GWh per year for an annual operating time of 6000 h. This estimate assumes linear scaling of the panel-level performance and neglects possible interactions between adjacent tunnel sections.

(a) (b)

Figure 5: Baseline (a) and optimised (b) fluid regions for the conductive block. A $\gamma = 0.95$ iso-contour is used to visualise the fluid domain.

3. Density-based topology optimization

The geometries of the brass conductive blocks in the conductive heat-recuperation unit and the serpentine layout in the radiative heat-recuperation unit were further improved by means of density-based topology optimisation [16]. In such an optimisation method, optimum material distribution (solid/fluid) is obtained in a predefined volumetric domain. Topology optimisation has been widely applied to the design of heat sinks, manifolds, and compact heat exchangers [17, 18]. In the scope of the current work, the objective was to increase heat recovery while limiting the pressure drop associated with the fluid flow. The design domain is represented as a porous medium described by a continuous design variable $\gamma \in [0, 1]$, where $\gamma = 0$ denotes solid material and $\gamma = 1$ denotes fluid. Intermediate values are allowed during the optimisation and progressively penalised to promote a nearly binary fluid–solid layout.

3.1. Conductive heat recuperation unit

Figure 5a shows the fluid domain of the conductive block used in the heat-recuperation unit, as used in modelling section. A CFD model of the baseline block was first established as the reference case for the optimisation study. The computational mesh was generated with Gmsh [19] and consists of approximately 2.84M tetrahedral elements. Simulations were performed with the SU2 CFD suite, extended with additional source terms to represent porous-medium flow and heat transfer [18]. Adiabatic boundary conditions are imposed on all external surfaces except for the lower face, where a uniform heat flux of $9.5\ \mathrm{kW\,m^{-2}}$ is prescribed. This value corresponds to the heat made available to a single block under the nominal operating conditions derived from the system-level analysis presented in Section 2.1.. The full set of boundary conditions is summarised in Table 2. For the primal and the adjoint solver, a CFL number of 20 was selected to ensure stable convergence. $\gamma = 0$ is imposed on the outer domain walls, whereas $\gamma = 1$ is imposed on the inlet and outlet pipe sections.

Turbulence is modelled with the SST k–ω model [20] following the porous-media approximation as detailed in Dilgen et al. [17]. Convective fluxes are discretised using a flux-difference-splitting scheme with MUSCL reconstruction [21], while the turbulence equations are solved using a scalar upwind discretisation. Spatial gradients are computed using a Green–Gauss formulation. The steady-state problem is advanced with an implicit Euler scheme, and the resulting linear systems are solved with FGMRES and ILU preconditioning [21]. With this setup, the baseline block yields an outlet-water temperature of $55.76\,^{\circ}\mathrm{C}$, corresponding to a temperature rise of $1.26\,^{\circ}\mathrm{C}$, and a pressure drop of 6.42 kPa.

The optimization framework used, is an extension of the FlowForge optimization framework described by [18]. The extensions are in terms of new objective functions. More specifically, in the

Table 2: Boundary conditions adopted for the CFD simulation of the baseline geometry. The same values are used in the optimisation study.

Parameter	**Value**	**Unit**
Inlet temperature	54.5	°C
Inlet velocity	0.51	m/s
Inlet mass flow rate	0.19	kg/s
Outlet pressure	1	bar
Heat flux at lower surface	9458	W/m^2
Fluid thermal conductivity	0.645	W/mK
Fluid heat capacity	4187	J/kgK
Solid thermal conductivity	109	W/mK

current work the optimisation problem is formulated as

$$\min_{\gamma} \quad \mathcal{J}(\gamma), \tag{1}$$

$$\text{s.t.} \quad g(\gamma) \leq 0, \tag{2}$$

where $\mathcal{J}(\gamma)$ is area-averaged temperature of the lower block surface, i.e. the surface in thermal contact with the coil, which can be defined as

$$\mathcal{J}(\gamma) = \frac{1}{A_{\text{bs}}} \int_{A_{\text{bs}}} T(\gamma)\, \mathrm{d}A \approx \frac{\sum_i T_i(\gamma_i)\, A_i}{A_{\text{bs}}}, \tag{3}$$

and $g_p(\gamma)$ is the pressure-drop constraint. where A_{bs} denotes the lower surface area of the block. Under fixed heat-flux conditions, lowering the interface temperature enhances heat extraction from the coil. The pressure-drop constraint is defined as

$$g(\gamma) = g_p(\gamma) = \frac{p_{\text{in}}(\gamma) - p_{\text{out}}(\gamma)}{\Delta p_{\text{ref}}} - 1, \tag{4}$$

where p_{in} and p_{out} are the inlet and outlet pressures, respectively, and Δp_{ref} is the reference pressure drop, taken equal to that of the baseline block.

The initial porosity field used in the optimisation consists of three rows of eight cylindrical pin-fin-like structures with a diameter equal to two-thirds of the inlet-channel diameter. To improve numerical robustness, a continuation strategy is adopted: the maximum penalisation factor for solid regions is fixed at $\alpha_{\max} = 200$, while the interpolation parameter q, which penalises intermediate porosity values, is gradually increased from 0.01 to 1 during the optimisation [18]. To suppress small geometrical features from the design and make it mesh-independent, a Helmholtz-type filter using a 5mm filter radius was applied to the optimisation variable field [22].

The constrained problem is solved using SNOPT [23] through pyOptSparse [24], with both optimality and feasibility tolerances set to 10^{-8}.

The optimization converged in approximately 300 design iterations. Figure 5b shows the optimised configuration of the conduction block. It can be observed that the fluid region extends over most of the lower heated surface, thereby increasing the area available for convective heat removal and reducing the mean temperature of the block-coil interface. The final topology also develops local recirculation zones near the lateral edges and along the centreline, giving rise to arch-like flow structures that promote mixing and improve local heat transfer.

Figure 6 shows the temperature fields on a plane located 15 mm above the lower surface for the baseline and optimised designs. In the optimised design, the temperature increases from inlet to outlet as the water progressively absorbs heat from the heated lower wall. The largest thermal non-uniformity appear near the outlet, where recirculating structures interact with the main flow path.

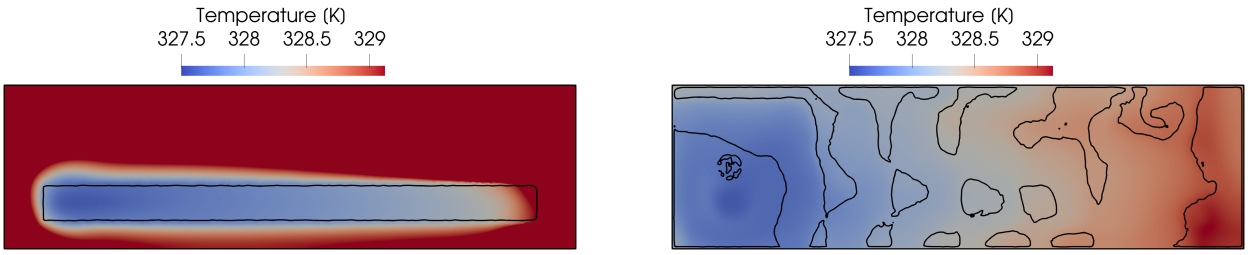

(a) (b)

Figure 6: Temperature fields for the baseline (a) and optimised (b) conductive-block design on a plane located 15 mm above the heated lower surface.

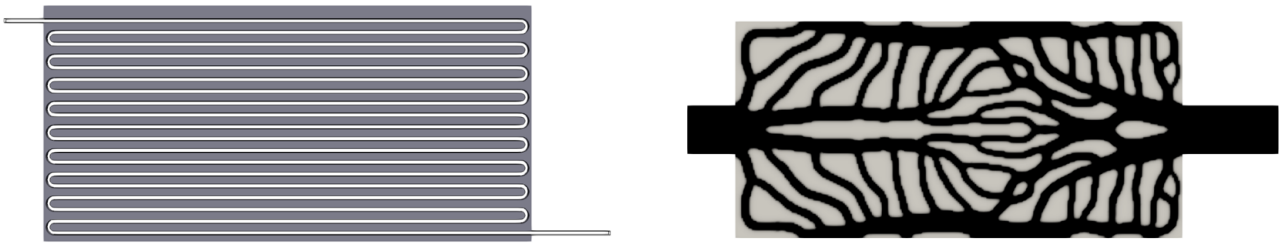

(a) (b)

Figure 7: Baseline (a) and optimised (b) layouts for the radiative panel. The black regions denote the fluid domain.

Thus a more uniform and lower average temperature across the plane ($\sim 10°\mathrm{C}$) is observed for the optimised design compared to the baseline design, thus minimising the heating of the metal.
For the optimised geometry, the outlet water temperature increases only marginally relative to the baseline case, whereas the pressure drop decreases by 26.5%. The limited improvement in outlet temperature is mainly a consequence of the relatively low heat flux imposed at the lower surface. Additional simulations indicate that the benefit of topology optimisation becomes more pronounced at higher heat-flux levels. This suggests that reducing the thermal-contact resistance between the coil and the brass block is at least as important as improving the internal flow topology. In practice, the full benefit of an optimised channel layout can only be realised if efficient thermal contact with the coil is maintained.

3.2. Radiative heat recuperation unit

Figure 7a shows the computational domain adopted for the optimisation of the radiative panel installed in the transport tunnel between the hot strip mill and the coil yard. To make the optimisation computationally feasible, the original geometry introduced in Section 2.2. was simplified in two ways. First, the serpentine was assumed to be embedded within the panel material rather than welded to its rear surface. Second, the inlet and outlet channels were modelled with a square cross-section of 200×15 mm instead of a circular diameter of 15 mm. These modifications enable a two-dimensional optimisation of the in-plane flow layout, which would not be feasible with the original serpentine configuration.
The optimum geometry obtained from the 2-dimensional problem was then simulated using a 3-dimensional conjugate heat-transfer simulation. In this case, fluid and solid were modeled independently and were coupled in SU2 through a multizone CHT formulation. At the fluid-solid interface, the coupling was enforced by prescribing a Dirichlet condition on the fluid side and a Robin condition on the solid side, following the approach of Pai Raikar et al [5]. No-slip conditions were applied at all fluid-solid walls. Local mesh refinement is applied to the walls in order to achieve $y^+ < 1$. A uniform heat flux of $2.89\ \mathrm{kW\,m^{-2}}$ was imposed on the heated lower surface, corresponding to a total heat load of 4.83 kW, consistent with the upper-panel value reported in Table 1b. All remaining exter-

nal walls were treated as adiabatic, while the other boundary conditions were taken from the baseline radiative-panel model described in Section 2.2.. The resulting performance of the adapted baseline design is reported in Table 3.

The panel was then optimised using a two-dimensional density-based topology-optimisation approach. To ensure robust convergence of both the primal and adjoint problems throughout the optimisation, the inlet and outlet sections were relocated to the panel centreline and widened to 0.2m. In addition, only half of the panel was simulated by exploiting mirror symmetry, thereby reducing the computational cost by approximately 50%. The optimisation framework and solver settings are the same as those adopted for the conductive block in Section 3.1.. The initial porosity field was set uniformly to $\gamma = 0.5$ over the entire design domain.

For this case, the objective function combines minimisation of the mean temperature in the domain and the pressure drop across the serpentine and is given as

$$\mathcal{J}(\gamma) = w_T \left[\frac{1}{V} \int_V T(\gamma)\, \mathrm{d}V \right] + w_p \big[p_{\mathrm{in}} - p_{\mathrm{out}}(\gamma) \big], \tag{5}$$

while the volume constraint is formulated as

$$g(\gamma) = g_{\mathrm{vol}}(\gamma) = \frac{\sum_i V_i\, \gamma_i}{fV} - 1. \tag{6}$$

Here, V is the total design-domain volume, T is the temperature, and w_T and w_p are the weighting coefficients of the thermal and hydraulic contributions, respectively. Following preliminary tests, the values $w_T = 0.99$ and $w_p = 0.01$ were retained. The volume constraint uses $f = 0.5$, corresponding to an equal target fraction of fluid and solid within the design domain.

Figure 7b shows the optimised flow layout obtained from the topology-optimisation procedure. In contrast to the baseline configuration, the optimised design branches into multiple flow paths, thereby increasing the coverage of the panel surface, reducing local velocities, and promoting more distributed heat removal.

To evaluate the performance of the optimised geometry and compare it with that of the baseline design, a fully body-fitted three-dimensional conjugate heat transfer (CHT) reconstruction of the optimised configuration was carried out. Separate meshes for the solid and fluid domains were generated from the porosity field resulting from the optimisation, using the same mesh refinement strategy adopted for the baseline design and applying the same boundary conditions as those defined in the optimisation problem.

Figure 8 presents the velocity and temperature fields for the baseline and optimised configurations. In the baseline case, heat removal is concentrated mainly in the transverse direction. By contrast, the optimised design promotes heat extraction along the panel's main longitudinal direction, thereby exploiting the larger panel dimension more effectively. In addition, the optimised topology strongly reduces the flow velocity: the maximum velocity is approximately one order of magnitude lower than in the baseline configuration, which explains the substantial reduction in pressure drop.

Table 3 compares the performance indicators of the baseline and optimised designs. Although the predicted outlet-water temperature of the optimised configuration is lower than that of the baseline case, the mean panel temperature and the overall thermal resistance are both reduced. This indicates that the optimised topology promotes more spatially uniform cooling of the panel and lowers the average panel temperature, even though the fluid experiences a smaller temperature rise along any individual flow path. At the same time, the pressure drop decreases from 2.52×10^3 Pa to 1.99 Pa, i.e. by more than three orders of magnitude. This large hydraulic improvement is directly consistent with the much lower flow velocities observed in the optimised configuration.

4. Conclusions

This work investigated two waste-heat recovery concepts for application in a steel production plant: a conductive heat-recuperation unit deployed directly on the hot coils in the coil yard, and a radiative

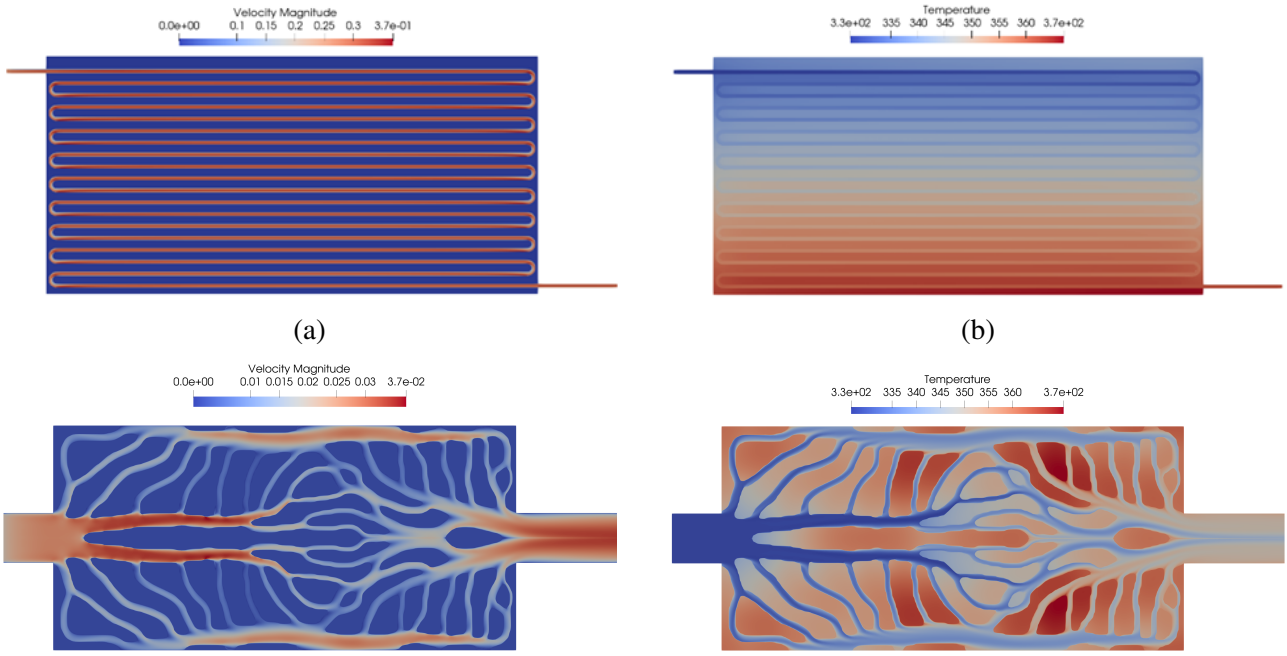

Figure 8: Velocity (left column) and temperature (right column) fields for the baseline (top row) and optimised (bottom row) radiative-panel configurations.

Table 3: Preliminary comparison of key performance indicators between the baseline and optimised radiative-panel designs.

Parameter	**Baseline**	**Optimised**	**Unit**
Outlet-water temperature	87.24	76.35	°C
Mean wall temperature ($\bar{T}_w$)	74.54	70.59	°C
Mean bulk temperature ($\bar{T}_b$)	70.87	68.85	°C
Thermal resistance	7.6×10^{-4}	6.0×10^{-4}	K/W
Pressure drop	2.52×10^{3}	1.99	Pa

heat-recuperation system installed along the transfer tunnel between the hot strip mill and the storage area. Based on the results of the system analysis and the design optimisation of key components of both heat recuperation units, the following conclusions can be drawn.

- Both concepts can contribute to industrial heat recuperation, but with different roles and recovery potentials. In particular, the conductive unit was found to recover a substantial amount of heat, reaching approximately 0.312 GWh per coil under the investigated operating conditions. The tunnel-based radiative system, instead, exhibited a much larger potential for large-scale recovery, estimated at around 13.1 GWh per year due to its continuous operation. Assuming heat recovery from 20 coils by conduction, together with radiation in the tunnel, the total recoverable energy is about 19.3 GWh per year.
- Topology optimisation can improve the hydraulic efficiency of both recovery systems without sacrificing thermal performance. For the conductive block, the optimised design reduced the pressure drop by 26%, whereas for the radiative panel, a three-order-of-magnitude reduction was achieved. These results confirm that adjoint-based, topology optimisation can support the development of energy-efficient components for waste heat recovery.

Overall, the paper shows that significant opportunities exist for recovering waste heat from steel coils, but also that heat recovery and cooling enhancement are not necessarily aligned objectives. Future work should therefore focus on industrial-scale validation, techno-economic assessment, and design

improvements aimed at increasing thermal contact and effective coverage if faster conductive cooling is to be pursued.

5. Acknowledgment

The research presented in this work was part of the Hurricane Project, supported by the European Union under the Horizon Europe funding programme with Grant Agreement No. 101138494. The authors gratefully acknowledge the CRM Group for providing the experimental data used in this study and for their valuable technical support. The computational resources and services used in this work were provided by the HPC core facility, CalcUA, of the Universiteit Antwerpen and VSC (Flemish Supercomputer Center), funded by the Research Foundation - Flanders (FWO) and the Flemish Government.

References

[1] World Steel Association, Sustainability indicators report 2025, reports sustainability performance of the steel industry, including 2024 data; accessed 16 March 2026 (Nov. 2025).
URL https://worldsteel.org/wider-sustainability/sustainability-indicators/

[2] H. Jouhara, S. Almahmoud, A. Chauhan, B. Delpech, G. Bianchi, S. A. Tassou, R. Llera, F. Lago, J. J. Arribas, Experimental and theoretical investigation of a flat heat pipe heat exchanger for waste heat recovery in the steel industry, Energy 141 (2017) 1928–1939. doi:10.1016/j.energy.2017.10.142.

[3] T. Borrvall, J. Petersson, Topology optimization of fluids in Stokes flow, International Journal for Numerical Methods in Fluids 41 (1) (2003) 77–107. doi:10.1002/fld.426.

[4] C. B. Dilgen, S. B. Dilgen, D. R. Fuhrman, O. Sigmund, B. S. Lazarov, Topology optimization of turbulent flows, Computer Methods in Applied Mechanics and Engineering 331 (2018) 363–393. doi:10.1016/j.cma.2017.11.029.

[5] P. Pai Raikar, N. Anand, M. Pini, C. De Servi, 3d optimization of heat sink fins using adjoint-based optimization with a CAD-based parametrization, International Journal of Heat and Mass Transfer 255 (2026) 127722. doi:10.1016/j.ijheatmasstransfer.2025.127722.

[6] National Metrology Institute of Japan, AIST, Network database system for thermophysical property data (tpds), free online database including thermal conductivity, thermal diffusivity, and heat capacity data for solids, liquids, and melts (2026).
URL https://tpds.db.aist.go.jp/opendata/data110401b_en.html

[7] A. F. Mills, C. F. M. Coimbra, Basic Heat and Mass Transfer, 3rd Edition, Temporal Publishing, LLC, 2015.

[8] S. W. Churchill, H. H. S. Chu, Correlating equations for laminar and turbulent free convection from a vertical plate, International Journal of Heat and Mass Transfer 18 (11) (1975) 1323–1329. doi:10.1016/0017-9310(75)90243-4.

[9] VDI Gesellschaft Verfahrenstechnik und Chemieingenieurwesen (GVC) (Ed.), VDI Heat Atlas, 2nd Edition, Springer, Berlin, Heidelberg, 2010. doi:10.1007/978-3-540-77877-6.

[10] C. F. Colebrook, C. M. White, Experiments with fluid friction in roughened pipes, Proceedings of the Royal Society of London. Series A, Mathematical and Physical Sciences 161 (906) (1937) 367–381. doi:10.1098/rspa.1937.0150.

[11] F. Ascione, P. Colonna, C. M. De Servi, Integrated design optimization method for novel vapour-compression-cycle-based environmental control systems, Applied Thermal Engineering 236 (2024) 121261. doi:10.1016/j.applthermaleng.2023.121261.

[12] H. Leuenberger, R. A. Person, Compilation of radiation shape factors for cylindrical assemblies,

ASME Paper 56-A-144, American Society of Mechanical Engineers, New York, NY (1956).

[13] E. J. LeFevre, A. J. Ede, Laminar free convection from the outer surface of a vertical cylinder, in: Proceedings of the 9th International Congress on Applied Mechanics, 1956, pp. 175–183.

[14] W. H. McAdams, Heat Transmission, 3rd Edition, McGraw-Hill, New York, 1954.

[15] M. V. Rane, M. S. Tandale, Water-to-water heat transfer in tube–tube heat exchanger: Experimental and analytical study, Applied Thermal Engineering 25 (17–18) (2005) 2715–2729. doi:10.1016/j.applthermaleng.2005.01.007.

[16] T. Matsumori, T. Kondoh, A. Kawamoto, T. Nomura, Topology optimization for fluid–thermal interaction problems under constant input power, Structural and Multidisciplinary Optimization 47 (4) (2013) 571–581. doi:10.1007/s00158-013-0887-8.

[17] S. B. Dilgen, C. B. Dilgen, D. R. Fuhrman, O. Sigmund, B. S. Lazarov, Density based topology optimization of turbulent flow heat transfer systems, Structural and Multidisciplinary Optimization 57 (5) (2018) 1905–1918. doi:10.1007/s00158-018-1967-6.

[18] S. Vermani, N. Anand, Density-based topology optimization strategy for optimal design of uniform flow manifolds, Computers & Fluids 302 (2025) 106847. doi:10.1016/j.compfluid.2025.106847.

[19] C. Geuzaine, J.-F. Remacle, Gmsh: A three-dimensional finite element mesh generator with built-in pre- and post-processing facilities, International Journal for Numerical Methods in Engineering 79 (11) (2009) 1309–1331. doi:10.1002/nme.2579.

[20] F. R. Menter, Two-equation eddy-viscosity turbulence models for engineering applications, AIAA Journal 32 (8) (1994) 1598–1605. doi:10.2514/3.12149.

[21] T. D. Economon, F. Palacios, S. R. Copeland, T. W. Lukaczyk, J. J. Alonso, SU2: An open-source suite for multiphysics simulation and design, AIAA Journal 54 (3) (2016) 828–846. doi:10.2514/1.J053813.

[22] B. S. Lazarov, O. Sigmund, Filters in topology optimization based on Helmholtz-type differential equations, International Journal for Numerical Methods in Engineering 86 (6) (2011) 765–781. doi:10.1002/nme.3072.

[23] P. E. Gill, W. Murray, M. A. Saunders, SNOPT: An SQP algorithm for large-scale constrained optimization, SIAM Review 47 (1) (2005) 99–131. doi:10.1137/S0036144504446096.

[24] E. Wu, G. Kenway, C. A. Mader, J. Jasa, J. R. R. A. Martins, pyOptSparse: A python framework for large-scale constrained nonlinear optimization of sparse systems, Journal of Open Source Software 5 (54) (2020) 2564. doi:10.21105/joss.02564.